Theoretical and Applied Mechanics Letters 12 (2022) 100349

Contents lists available at ScienceDirect

Theoretical and Applied Mechanics Letters

journal homepage: www.elsevier.com/locate/taml

Letter

Independent component analysis of streamwise velocity fluctuations in turbulent channel flows

Ting Wu [a,b], Guowei He [a,b,*]

[a] The State Key Laboratory of Nonlinear Mechanics, Institute of Mechanics, Chinese Academy of Sciences, Beijing 100190, China
[b] School of Engineering Sciences, University of Chinese Academy of Sciences, Beijing 100049, China

ARTICLE INFO

Article history:
Received 24 May 2022
Accepted 26 May 2022
Available online 3 June 2022

Keywords:
Independent component analysis
Turbulent channel flow
Proper orthogonal decomposition
Third-order moment
Localised modes

ABSTRACT

Independent component analysis (ICA) is used to study the multiscale localised modes of streamwise velocity fluctuations in turbulent channel flows. ICA aims to decompose signals into independent modes, which may induce spatially localised objects. The height and size are defined to quantify the spatial position and extension of these ICA modes, respectively. In contrast to spatially extended proper orthogonal decomposition (POD) modes, ICA modes are typically localised in space, and the energy of some modes is distributed across the near-wall region. The sizes of ICA modes are multiscale and are approximately proportional to their heights. ICA modes can also help to reconstruct the statistics of turbulence, particularly the third-order moment of velocity fluctuations, which is related to the strongest Reynolds shear-stress-producing events. The results reported in this paper indicate that the ICA method may connect statistical descriptions and structural descriptions of turbulence.

Turbulence is composed of flow structures at different scales. Spatially localised structures have important applications in turbulent cascades [1], wall turbulence dynamics [2,3] and aerodynamic noise [4]. However, the structure of turbulence still lacks a commonly accepted definition, and extracting spatially localised structures at different scales from flow data remains challenging [5].

One type of flow structure analysis method is vortex identification criteria, such as the Q criterion [6], Δ criterion [7], λ_2 criterion [8], etc. Most of these methods are based on local flow kinematics implied by the velocity gradient tensor and can identify spatially localised structures, such as vortex worms in isotropic turbulence [9] and hairpin vortices in wall turbulence [10].

Others type of flow structure analysis method includes Fourier analysis, proper orthogonal decomposition (POD) [11], and wavelet analysis [12], which decompose a flow into modes at different scales. Fourier analysis is used in homogeneous turbulence, and POD is a generalization of Fourier analysis in inhomogeneous turbulence [13]. Both Fourier analysis and POD consider the energy and Reynolds stress of a flow globally so that their modes are spatially extended. Wavelet analysis uses localized basis functions and can estimate the multiscale characteristics of the flow at different spatial positions [14].

In addition, Schmid [15] proposed dynamic mode decomposition (DMD) to capture the dynamics of flow fields. The DMD method can extract modes with different temporal properties (i.e., frequencies and growth rates). Thus, the DMD method can effectively analyse flows that contain multiple instability mechanisms.

Recently, the empirical mode decomposition (EMD) method [16] has been applied in turbulence research. Agostini and Leschziner [17,18] used bidimensional EMD (BEMD) to analyse the effect of large-scale structures on near-wall turbulence. EMD partitions the instantaneous flow into modes (IMFs, intrinsic mode functions) without relying on a priori basis functions; thus, EMD is an adaptive multiscale analysis method.

In addition to these methods, independent component analysis (ICA) has been developed to decompose mixed signals into independent components and is widely used in data analysis, such as predicting stock market prices [19] and analyzing RNA-sequencing experiments [20]. Carassale [21] used ICA in turbulent flows and described the difference between POD and ICA modes.

In this paper, we use ICA to analyse the localised multiscale modes in turbulent channel flows. We have two motivations for using ICA to analyse turbulence data. On one hand, independence may lead to the spatial locality of modes. If two structures are spa-

* Corresponding author.
E-mail address: hgw@lnm.imech.ac.cn (G.W. He).

https://doi.org/10.1016/j.taml.2022.100349

tially localised (i.e., their intersection in space is relatively small), then they are more likely to be independent. In contrast, if two structures are spatially extended (i.e., their intersection in space is relatively large), then they are less likely to be independent. Jiménez [5] reported a similar explanation while considering the turbulent boundary layer over a wing. Therefore, spatial locality may be achieved through independence of modes. On the other hand, independence itself is also important to describe the statistical properties of turbulence. Mouri [22] described the kinetic energy, Reynolds stress and two-point correlations in wall turbulence by assuming the randomness and independence of the attached eddies. Therefore, ICA may be able to connect statistical descriptions and structural descriptions of turbulence.

Considering an observed multidimensional variable $\mathbf{o}$, ICA assumes that the variable $\mathbf{o}$ can be written as [23]:

$$\mathbf{o} = \mathbf{A}\mathbf{s}, \tag{1}$$

where $\mathbf{o} = [o_1, o_2, \cdots, o_n]^{\mathrm{T}}$ is the observed signal, $\mathbf{s} = [s_1, s_2, \cdots, s_n]^{\mathrm{T}}$ is a set of mutually independent source signals, and $\mathbf{A}$ is a linear mixing matrix, indicating that the observed signals o_i are linear mixtures of independent source signals $\mathbf{s}$. The task of ICA is to find the maximum independent set of source signals $\mathbf{s}$ and the mixing matrix $\mathbf{A}$ for the given observed signals $\mathbf{o}$. Because both $\mathbf{s}$ and $\mathbf{A}$ are unknown, we can arbitrarily change the magnitudes and the order of source signals and suitably change the corresponding columns of $\mathbf{A}$ to generate the same observed signals. Thus, there are ambiguities in the magnitudes and the order of the independent components [23]. To eliminate these ambiguities, we assume that the source signals exhibit unit variances [24] and thus arrange the source signals by their heights.

In the ICA model, mutual information is used to measure the dependence between random variables. The mutual information between n random variables s_i $(i = 1, 2, \cdots, n)$ is defined as:

$$I(s_1, s_2, \cdots, s_n) = \sum_{i=1}^{n} H(s_i) - H(\mathbf{s}), \tag{2}$$

where $H(\cdot)$ is the differential entropy of the random variable:

$$H(\mathbf{s}) = -\int p(\mathbf{s}) \ln p(\mathbf{s}) \mathrm{d}\mathbf{s}, \tag{3}$$

$$H(s_i) = -\int p(s_i) \ln p(s_i) \mathrm{d}s_i. \tag{4}$$

where $p(s_i)$ is the probability density function (PDF) of random variable s_i, and $p(\mathbf{s})$ is the PDF of random vector $\mathbf{s}$. Because $p(\mathbf{s})$ is an n-dimensional joint PDF, $H(\mathbf{s})$ is difficult to estimate directly. Some pre-processing techniques, such as the whitening transformation, can simplify the estimation of the differential entropy $H(\mathbf{s})$. Mutual information is always nonnegative and equals zero if and only if the variables s_i are mutually independent. Therefore, mutual information is a natural measure for independence, and the goal of ICA is to minimize the mutual information between the components (i.e., maximize the independence between the source signals).

There are various ICA algorithms, such as Infomax [25], FastICA [26], and MISEP [27]. In this study, we use the FastICA algorithm, which is described in detail by Hyvärinen and Oja [24] and is implemented in Scikit-learn [28]. The Infomax algorithm is also used, and its results are similar to those of FastICA and thus not reported.

Considering the n-dimensional zero-mean vector $\mathbf{o}$, its covariance matrix is:

$$\mathbf{R} = \langle \mathbf{o}\mathbf{o}^{\mathrm{T}} \rangle, \tag{5}$$

where the angular bracket $\langle \cdot \rangle$ denotes the mathematical expectation, and the superscript "T" indicates the transpose. According to POD, $\mathbf{o}$ can be represented by the modal expansion:

$$\mathbf{o} = \sum_{i=1}^{n} c_i \mathbf{q}_i, \tag{6}$$

where c_i $(i = 1, 2, \cdots, n)$ are the modal coefficients and the vectors $\mathbf{q}_i$ $(i = 1, 2, \cdots, n)$ are the POD modes that are the eigenvectors of the covariance matrix:

$$\mathbf{R}\mathbf{q}_i = \lambda_i \mathbf{q}_i. \tag{7}$$

Among all available linear decompositions, POD is the most efficient in the sense of containing kinetic energy for a given number of modes if o refers to the velocity. Thus, POD is often used to derive reduced-order models. POD modes are orthonormal (i.e. $\mathbf{q}_i^{\mathrm{T}}\mathbf{q}_j = \delta_{ij}$), and the POD coefficients are uncorrelated:

$$\langle c_i c_j \rangle = 0 \quad \text{for} \quad i \neq j. \tag{8}$$

According to Eq. (1), the ICA model can be rewritten as:

$$\mathbf{o} = \sum_{i=1}^{n} s_i \mathbf{g}_i, \tag{9}$$

where $\mathbf{g}_i$ is the ith column vector of the mixing matrix $\mathbf{A}$. The source signal s_i is the coefficient of the ICA mode $\mathbf{g}_i$. Due to the independence of s_i, we have:

$$\langle s_i s_j \rangle = \langle s_i \rangle \langle s_j \rangle = 0 \quad \text{for} \quad i \neq j, \tag{10}$$

Thus, the independent variables are uncorrelated. However, uncorrelatedness does not imply independence. Thus, the ICA modes are more advantageous in reconstructing higher-order statistics. Considering the third-order moment as an example, we have $\langle s_i^2 s_j \rangle = 0$ $(i \neq j)$ for the ICA coefficients, but there is no guarantee that $\langle c_i^2 c_j \rangle = 0$ $(i \neq j)$ for the POD coefficients.

Considering the wall-normal profile of streamwise velocity fluctuations $u(y; x, z, t)$ in the turbulent channel flows, x, y and z denote the coordinates in the streamwise, wall-normal and spanwise directions, respectively; and t denotes the time. We only discuss the wall-normal modes in this paper and not the three-dimensional modes because the ICA model of three-dimensional modes is difficult to formulate into a well-defined and solvable form. The flow structures in turbulent channels can move randomly in the streamwise and spanwise directions together with the downstream convection. If the three-dimensional ICA modes characterize these randomly moving structures, the ICA model can be expressed as:

$$u(y; x, z, t) = \sum_{i=1}^{n} s_i(t) u_i^{\mathrm{ICA}}(x - x_c(t), y, z - z_c(t)), \tag{11}$$

where $u_i^{\mathrm{ICA}}(x - x_c(t), y, z - z_c(t))$ is the ICA mode centred at $x_c(t)$ and $z_c(t)$ in the streamwise and spanwise directions, respectively; and $x_c(t)$ and $z_c(t)$ depend on t because the spatially localised structures in turbulent channels should be moving. The ICA model defined by Eq. (11) is difficult to solve, particularly because the properties of $x_c(t)$ and $z_c(t)$ are unknown. If we simply write the ICA model as:

$$u(y; x, z, t) = \sum_{i=1}^{n} s_i(t) u_i^{\mathrm{ICA}}(x, y, z), \tag{12}$$

then the ICA modes $u_i^{\mathrm{ICA}}(x, y, z)$ are spatially fixed, which is not reasonable for structures in turbulent channels.

There are n grid points from the wall to the centre of the channel in the wall-normal direction, and the coordinates of these grid points are y_j, where $j = 1, 2, \cdots, n$. We represent $u(y; x, z, t)$ as a mixture of ICA modes:

$$u(y; x, z, t) = \sum_{i=1}^{n} s_i(x, z, t) u_i^{\mathrm{ICA}}(y), \tag{13}$$

where $u_i^{\mathrm{ICA}}(y)$ is the ith ICA mode, and the coefficients s_i of these modes maximize independence. In this paper, we only study the multiscale localised modes in the wall-normal direction; thus, x, z and t only serve to increase the number of samples.

We first obtain the POD modes of the streamwise velocity fluctuations by:

$$\int_0^h R(y,y')u_j^{\mathrm{POD}}(y')\mathrm{d}y' = \lambda_j u_j^{\mathrm{POD}}(y), \tag{14}$$

where h is the half-height of the channel, $u_j^{\mathrm{POD}}(y)$ denotes the jth POD mode, $R(y,y') = \langle u(y;x,z,t)u(y';x,z,t)\rangle$ is the two-point correlation in the wall-normal direction, and the angular bracket $\langle\cdot\rangle$ denotes the ensemble average, which is performed in time and in the streamwise and spanwise directions due to homogeneity. Then, the velocity field can be represented by the POD modes:

$$u(y;x,z,t) = \sum_{j=1}^{n} o_j(x,z,t)u_j^{\mathrm{POD}}(y), \tag{15}$$

where o_j is the coefficient of the jth POD mode. When the dimension n is large, we can neglect some POD modes that have little energy and use an appropriate number of modes to perform the following ICA decomposition, thereby reducing the dimension and making the ICA simpler.

Assuming that o_j can be expressed as an ICA model:

$$o_j(x,z,t) = \sum_{i=1}^{n} A_{ji}s_i(x,z,t), \tag{16}$$

where o_j denotes the observed signal, which can be obtained by Eq. (15); s_i $(i = 1,2,\cdots,n)$ are independent source signals; and A_{ji} is the element in the mixing matrix. Substituting Eq. (16) into Eq. (15) yields:

$$u(y;x,z,t) = \sum_{i=1}^{n} s_i(x,z,t)\left[\sum_{j=1}^{n} A_{ji}u_j^{\mathrm{POD}}(y)\right]. \tag{17}$$

Thus, we can obtain n ICA modes as:

$$u_i^{\mathrm{ICA}}(y) = \sum_{j=1}^{n} A_{ji}u_j^{\mathrm{POD}}(y). \tag{18}$$

This ICA procedure can be used for other variables, such as pressure and streamwise vorticity, and for all three velocity components, in which the POD modes of one velocity component must be replaced with the POD modes of all velocity components.

Some ICA modes described by Eq. (18) are not smooth and have small amplitudes, which can be considered as noise. To discard these noise modes, we define the following regularization criterion based on the local energy ratio:

$$\rho_i = \max_{y\in(0,h]} \frac{\langle s_i^2\rangle [u_i^{\mathrm{ICA}}(y)]^2}{\sum_{j=1}^{n}\langle s_j^2\rangle [u_j^{\mathrm{ICA}}(y)]^2}, \tag{19}$$

ρ_i is the maximum ratio of the energy of the ith ICA mode to the local total energy at different wall-normal positions. A small ρ_i implies that the ith ICA mode can be ignored at all wall-normal positions; then, this mode can be discarded. In this paper, we regard the modes of $\rho_i < 0.05$ as noise and only retain the modes of $\rho_i \geq 0.05$. We assume that m modes remain after the regularization, and the indices of these modes are $i = 1,2,\cdots,m$. The velocity field can be exactly reconstructed by n linearly uncorrelated modes, and m modes after regularization can only approximately reconstruct the velocity field:

$$u^{\mathrm{ICA}}(y_j;x,z,t) = \sum_{i=1}^{m} u_i^{\mathrm{ICA}}(y_j){s'}_i(x,z,t), \tag{20}$$

where $u^{\mathrm{ICA}}(y_j;x,z,t)$ is the approximate velocity field reconstructed by m ICA modes and s'_i is the modified coefficient. The velocity field of each mode in the channel is:

$$u_i^{\mathrm{ICA}}(y;x,z,t) = u_i^{\mathrm{ICA}}(y)s'_i(x,z,t). \tag{21}$$

The reconstructed velocity field can be written as the sum of the contributions of the m ICA modes:

$$u^{\mathrm{ICA}}(y;x,z,t) = \sum_{i=1}^{m} u_i^{\mathrm{ICA}}(y;x,z,t). \tag{22}$$

We let $N_{ji} = u_i^{\mathrm{ICA}}(y_j)$ and the matrix $\mathbf{N} = (N_{ji})_{n\times m}$; then:

$$u^{\mathrm{ICA}}(y_j;x,z,t) = \sum_{i=1}^{m} N_{ji}{s'}_i(x,z,t). \tag{23}$$

To make the reconstructed velocity field $u^{\mathrm{ICA}}(y_j;x,z,t)$ a good approximation of $u(y_j;x,z,t)$, we determine the modified coefficient as:

$$s'_i(x,z,t) = \sum_{j=1}^{n} Q_{ij}u(y_j;x,z,t), \tag{24}$$

where $(Q_{ij})_{m\times n} = \mathbf{N}^{+}$, and "+" in this study indicates the Moore-Penrose pseudoinverse, which provides a least-squares solution to a system of linear equations that lacks a unique solution [29].

In the next section, the ICA modes $u_i^{\mathrm{ICA}}(y)$ for the wall-normal profile of the streamwise velocity fluctuations will be obtained using the above procedure.

In this study, we use datasets from the direct numerical simulation (DNS) of turbulent channel flows at $\mathrm{Re}_\tau \equiv u_\tau h/\nu = 205$, where u_τ is the friction velocity, h is the half-height of the channel and ν is the kinematic viscosity. The pseudospectral method is used to solve the Navier-Stokes equation, and the 3/2 rule is used to remove aliasing errors. Periodic boundary conditions are used in the streamwise and spanwise directions, and no-slip boundary conditions are used at the bottom and top walls. The computational domain is $1.3\pi h \times 2h \times 0.35\pi h$, and the grid numbers $64 \times 129 \times 32$ are used in the streamwise (x), wall-normal (y), and spanwise (z) directions. The time step to advance the Navier-Stokes equations is considered to be $\Delta t^{+} = 0.012$, and "+" indicates normalization with viscous scales. The Navier-Stokes solver and the datasets used in this study have been validated in previous studies [30].

One hundred snapshots of the instantaneous streamwise velocity fluctuations are used. Because we only investigate the wall-normal modes from the wall to the centre of the channel, not the modes between two walls, the total number of samples for the ICA procedure is 409,600 ($64 \times 32 \times 100 \times 2$). The velocity at the wall is zero, and the grid point at the wall is therefore not considered in the POD and ICA; there are also 64 grid points in the wall-normal direction. Therefore, 64 POD modes and 64 ICA modes are obtained according to the procedure. With regularization, 33 ICA modes remain. To test whether the 33 ICA modes can reconstruct the velocity field well, we define the relative error of the reconstructed velocity field:

$$\varepsilon(y) = \frac{\langle [u^{\mathrm{ICA}}(y;x,z,t) - u(y;x,z,t)]^2\rangle}{\langle u^2(y;x,z,t)\rangle}. \tag{25}$$

Results show that the relative error $\varepsilon(y)$ is less than 0.2% at all positions and less than 0.1% at most positions; thus, the 33 ICA modes can be used to reconstruct the velocity field well.

Figure 1 a plots the velocity profile of four POD modes with $i = 1,3,6,9$, and Fig. 1b plots the velocity profile of four ICA modes with $i = 5,11,17,24$. The POD modes are spatially extended and oscillatory throughout the region, similar to the trigonometric functions in Fourier analysis. While the ICA modes are spatially localised, particularly for those modes whose peaks are near

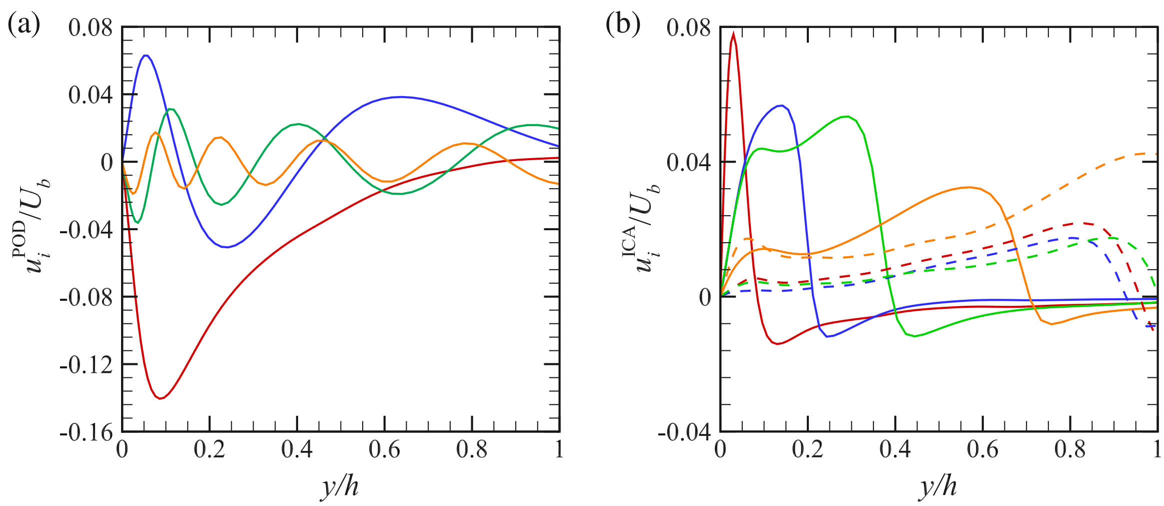

Fig. 1. (**a**) Velocity profile of four POD modes with $i = 1, 3, 6, 9$. (**b**) Velocity profile of eight ICA modes with $i = 5, 11, 17, 24$ (solid lines) and $i = 30, 31, 32, 33$ (dashed lines).

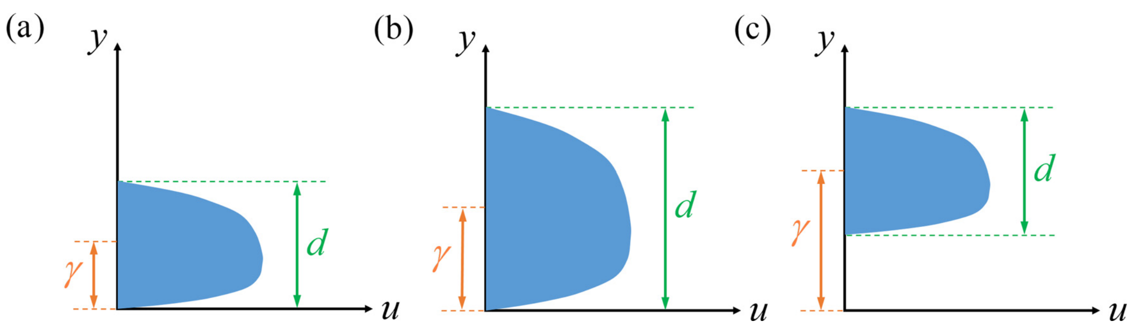

Fig. 2. Schematic of the height and size of the ICA mode.

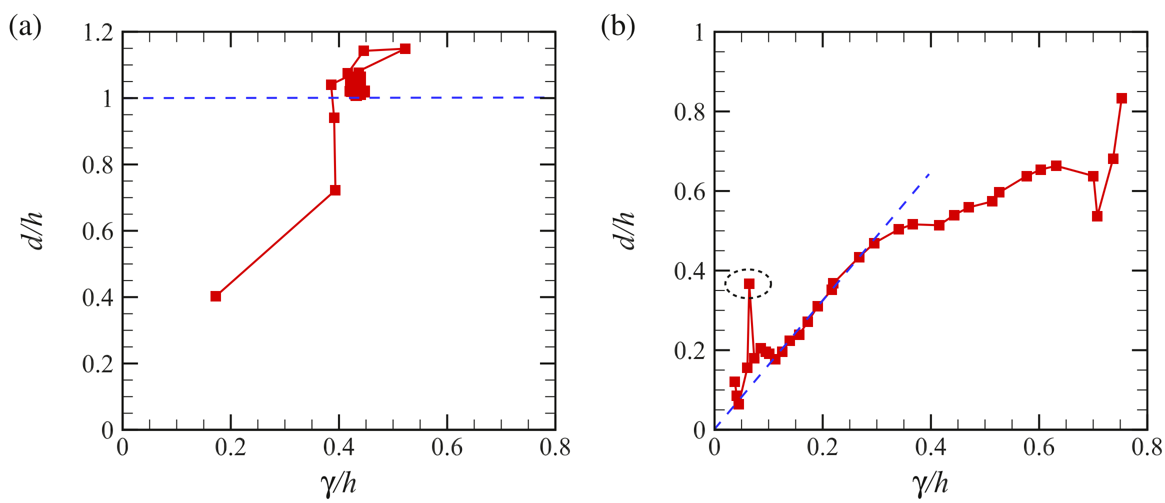

Fig. 3. (**a**) Sizes of the first 33 POD modes vary with height. The blue dashed line indicates that the size is h. (**b**) Sizes of the ICA modes vary with height. The blue dashed line indicates that the size is proportional to the height, and the black dotted circle indicates the ICA mode with $i = 5$.

the wall, the amplitudes of these modes asymptotically tend toward zero at the centre of the channel. In addition, there are some modes whose peaks are near the centreline, and these modes contribute to the fluctuations at the centre of the channel. Figure 1b implies that spatial locality may indeed be induced by independence, which can be described as follows. If two structures are localised in space (i.e., their intersection is relatively small), then they are more likely to be independent. In contrast, if two structures are spatially extended (i.e., their intersection in space is relatively large), then they are less likely to be independent. Therefore, the ICA method provides a path to obtain spatially localised structures.

To quantify the spatial extension of a mode, the height γ and size d are defined as two characteristic length scales. The height of a mode $u_i(y)$ is defined as:

$$\gamma_i = \frac{\int_0^h y[u_i(y)]^2 \mathrm{d}y}{\int_0^h [u_i(y)]^2 \mathrm{d}y}, \tag{26}$$

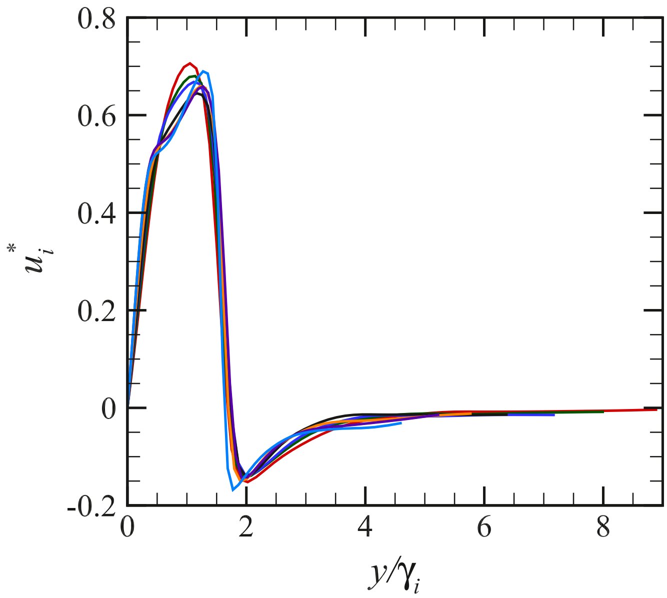

Fig. 4. Normalized velocity profile of the ICA modes with $i = 10, 11, \cdots, 16$.

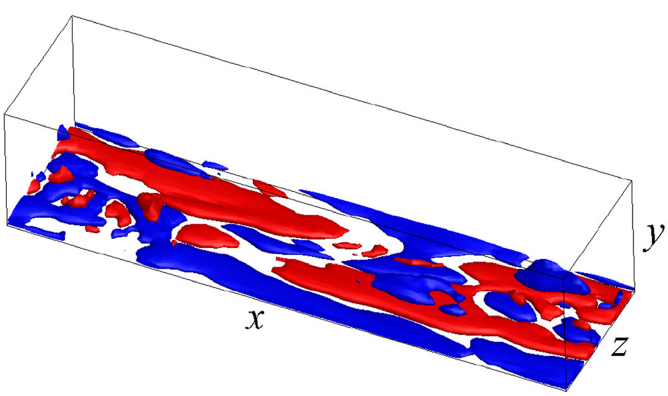

Fig. 5. Instantaneous isosurfaces of the streamwise velocity fluctuations of the ICA mode with $i = 5$. The blue coloured objects are low-velocity streaks, $u_5^{\mathrm{ICA}}(y; x, z, t)/u_\tau = -0.5$. The red coloured objects are high-velocity streaks, $u_5^{\mathrm{ICA}}(y; x, z, t)/u_\tau = 0.5$.

where γ_i represents the energy-weighted wall distance of the ith mode. The size of a mode $u_i(y)$ is defined as:

$$d_i = 2\sqrt{3}\sqrt{\frac{\int_0^h (y-\gamma_i)^2 [u_i(y)]^2 \mathrm{d}y}{\int_0^h [u_i(y)]^2 \mathrm{d}y}}, \tag{27}$$

where d_i represents the energy-weighted spatial extension of the ith mode. If the energy of a mode is uniformly distributed in the region $[0, h]$, the size of the mode is calculated as h according to Eq. (27). Figure 2 shows sketches of the height and size of a mode. Both the height and size of the mode shown in Fig. 2b are larger than those shown in Fig. 2a. Although the height of the mode in Fig. 2c is larger than that in Fig. 2a, the two modes have the same size. As mentioned before, the order of the independent components cannot be determined by the ICA procedure [23]; thus, we sorted the ICA modes according to their heights from small to large.

Figure 3 a plots the sizes of the first 33 POD modes with the heights. The sizes of most POD modes are h, which means that the energy of most POD modes is distributed throughout the region $[0, h]$; thus, the POD modes approximate the velocity field in a global sense. Figure 3b plots the sizes of ICA modes with the heights. The sizes of most ICA modes are smaller than those of POD modes, indicating the spatial locality of ICA modes. In addition, the sizes of ICA modes exhibit a multiscale nature and are approximately proportional to the heights, particularly the modes with $i = 10, 11, \cdots, 16$. We define the normalized velocity profile of the ICA mode:

$$u_i^*(y) = u_i^{\mathrm{ICA}}(y)\sqrt{\frac{d_i}{\int_0^h [u_i^{\mathrm{ICA}}(y')]^2 \mathrm{d}y'}}. \tag{28}$$

Figure 4 plots the normalized velocity profile of the ICA modes with $i = 10, 11, \cdots, 16$, where the wall distance y is normalized by the height of each mode. A good collapse is shown in Fig. 4, highlighting the similarity of these ICA modes. This collapse implies that the height is the characteristic length scale of an ICA mode.

The mode with $i = 5$ is special and is marked by the black dotted circle in Fig. 3b; its size is much larger than other modes at the height $\gamma_5^+ \approx 13$ in the buffer layer. Figure 5 plots the instantaneous isosurfaces of the streamwise velocity fluctuations of the ICA mode with $i = 5$. Streamwise elongated streaks are also shown. Figure 6a plots the velocity profile of the ICA mode with $i = 5$. The positions with large amplitudes of this mode are in the region of $y^+ < 30$; thus, this mode primarily exists in the buffer layer. We then calcu-

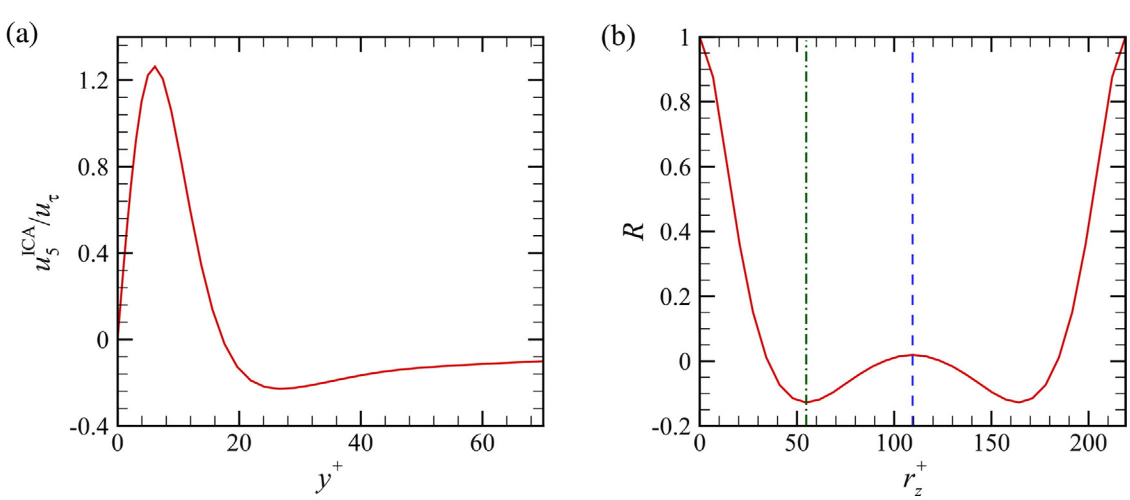

Fig. 6. (**a**) Velocity profile of the ICA mode with $i = 5$. (**b**) Spanwise correlation of the ICA mode with $i = 5$. The blue dashed line indicates the local maximum correlation, and the green dash-dotted line indicates the minimum correlation.

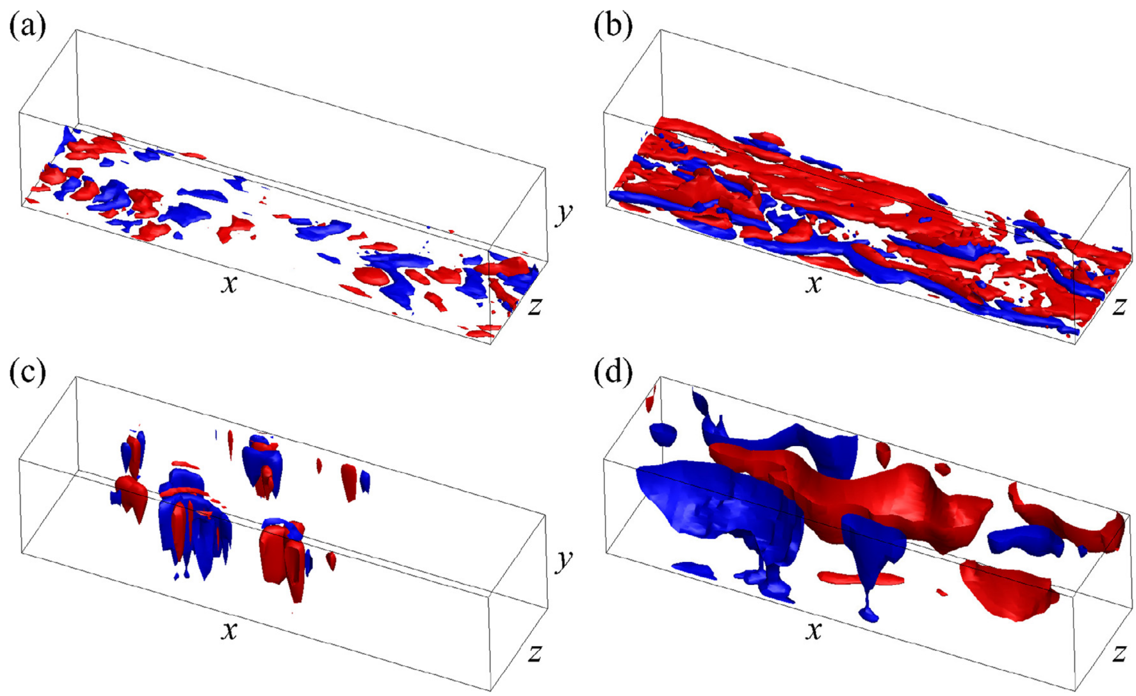

Fig. 7. Instantaneous isosurfaces of the streamwise velocity fluctuations of four ICA modes. The blue coloured isosurfaces, $u_i^{\mathrm{ICA}}(y;x,z,t)/u_\tau = -0.5$. The red-coloured isosurfaces, $u_i^{\mathrm{ICA}}(y;x,z,t)/u_\tau = 0.5$. (**a**) $i=1$; (**b**) $i=7$; (**c**) $i=30$; (**d**) $i=33$.

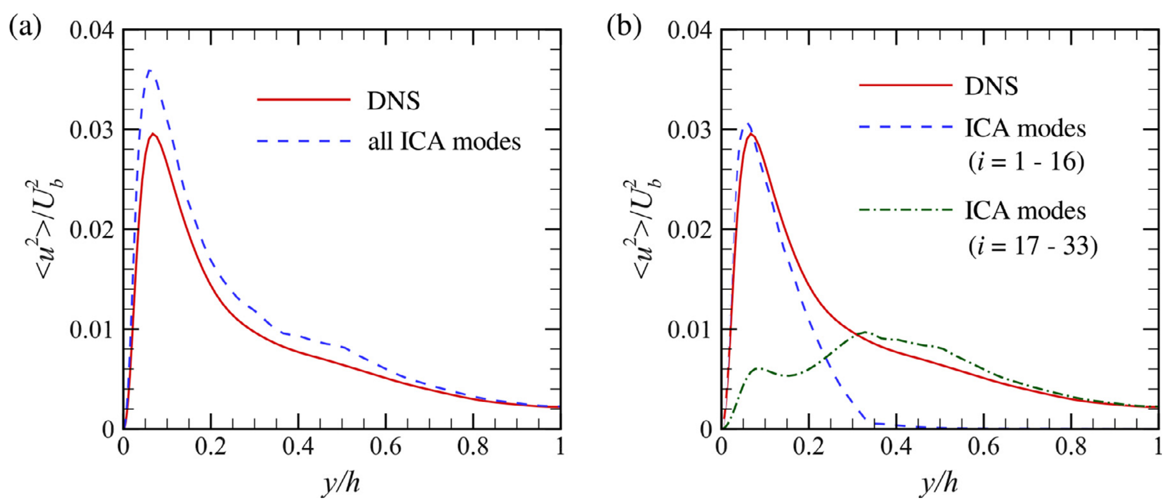

Fig. 8. (**a**) Sum of the second-order moments of all ICA modes compared with the DNS result of streamwise velocity fluctuations. (**b**) Sum of the second-order moments of ICA modes with $i = 1, 2, \cdots, 16$ and with other ICA modes.

late the spanwise correlation of this mode:

$$R_i(r_z) = \frac{\langle s'_i(x,z,t)s'_i(x,z+r_z,t)\rangle}{\langle s'_i(x,z,t)s'_i(x,z,t)\rangle}. \tag{29}$$

Figure 6b plots the spanwise correlation of the ICA mode with $i=5$. The mean spanwise spacing between the adjacent low- and high-speed streaks is $\lambda_z^+ \approx 55$ according to the minimum of the spanwise correlation, which is consistent with $\lambda_z^+ \approx 50$ in Kim et al. [31]. The mean spanwise spacing between two adjacent low-speed or high-speed streaks is $\lambda_z^+ \approx 110$ according to the local maximum of the spanwise correlation, which is consistent with $\lambda_z^+ \approx 100$ in Smits et al. [32].

Figure 7 plots the instantaneous isosurfaces of two near-wall ICA modes with $i=1,7$ and two outer ICA modes with $i=30,33$. The isosurfaces of $i=1$ and $i=30$ are disrupted and irregular, which are markedly different from the streamwise streaks of the $i=5$ mode. The isosurfaces of $i=7$ and $i=33$ are elongated in the streamwise direction, similar to the streamwise streaks, but their spanwise spacing is larger than that of the $i=5$ mode.

If the ICA modes are strictly independent, we have the following equations for turbulence statistics:

$$\langle u^2(y)\rangle = \sum_i \langle s'^2_i\rangle [u_i^{\mathrm{ICA}}(y)]^2, \tag{30}$$

$$R(y,y') = \sum_i \langle s'^2_i\rangle u_i^{\mathrm{ICA}}(y) u_i^{\mathrm{ICA}}(y'), \tag{31}$$

$$\langle u^3(y)\rangle = \sum_i \langle s'^3_i\rangle [u_i^{\mathrm{ICA}}(y)]^3. \tag{32}$$

Figure 8 a plots the sum of the second-order moments of all ICA modes compared with the DNS result of streamwise velocity fluctuations. The two results are similar, which comes from the approximate independence between these modes. Figure 8b

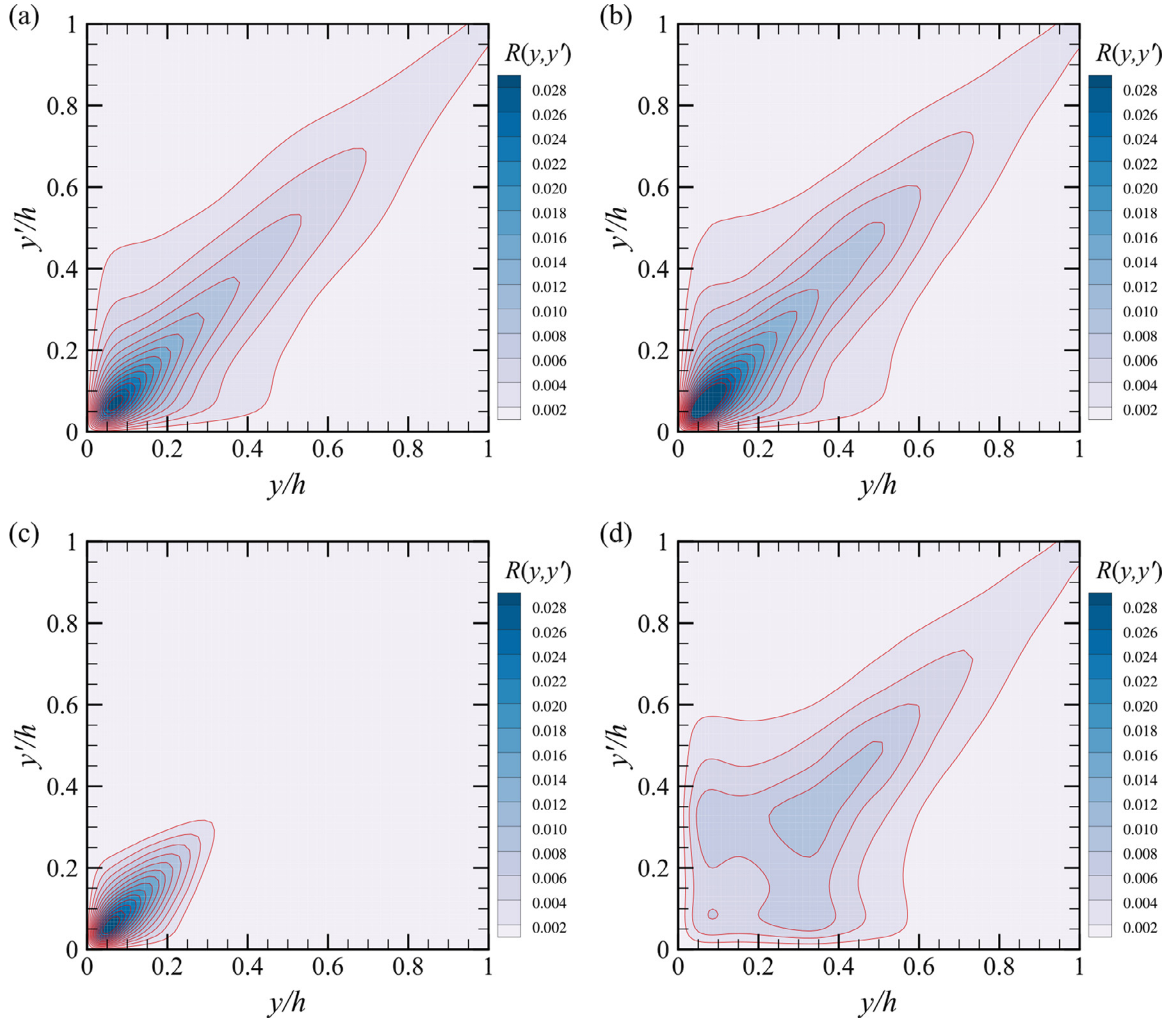

Fig. 9. (**a**) DNS result of the wall-normal correlation of streamwise velocity fluctuations. (**b**) Sum of the wall-normal correlation of all ICA modes. (**c**) Sum of the wall-normal correlation of ICA modes with $i = 1, 2, \cdots, 16$. (**d**) Sum of the wall-normal correlation of ICA modes with $i = 17, 18, \cdots, 33$.

plots the sum of the second-order moments of ICA modes with $i = 1, 2, \cdots, 16$ and with other ICA modes. The energy of modes with $i = 1, 2, \cdots, 16$ is distributed across the near-wall region. Figure 9a plots the DNS result of the wall-normal correlation of streamwise velocity fluctuations. Figure 9b plots the sum of the wall-normal correlation of all ICA modes. These two results are similar. Figure 9c plots the sum of the wall-normal correlation of ICA modes with $i = 1, 2, \cdots, 16$, and Fig. 9d plots the result with other ICA modes. The wall-normal correlation of ICA modes with $i = 1, 2, \cdots, 16$ is distributed in the near-wall region, which further shows the spatial locality of the ICA modes.

Figure 10a plots the sum of the third-order moments of all ICA modes and that of all POD modes compared with the DNS result. The DNS third-order moment is positive in the near-wall region and negative in the other region. The behaviour of the third-order moment is expected from the quadrant analysis and the most violent Reynolds shear-stress-producing events [31]; thus, the strongest Reynolds shear-stress-producing events are the ejection events ($u' < 0$) for $y^+ > 12$; sweep events also occur ($u' > 0$) for $y^+ < 12$. The sum of the third-order moments of all ICA modes has this feature, while that of all POD modes does not. The sum of the third-order moments of all POD modes is always negative throughout the region. Therefore, compared with POD, the ICA method is better for the higher-order statistics of turbulence. As mentioned before, the obtained ICA modes are not completely independent; thus, the sum of the third-order moments of all ICA modes is not exactly equal to the DNS result. Figure 10b plots the sum of the third-order moments of ICA modes with $i = 1, 2, \cdots, 5$ and with other modes. The modes with $i = 1, 2, \cdots, 5$ contribute to the positive third-order moment in the near-wall region, and the other modes contribute to the negative third-order moment.

In this paper, the ICA method is used to decompose the wall-normal profile of the streamwise velocity fluctuations in turbulent channel flows. ICA aims to decompose the signals into independent components, and the spatial locality may be induced independently. Therefore, spatially localised structures in turbulence may be obtained by the ICA method.

Using the DNS data of the turbulent channel flows at $Re_\tau = 205$, we find that ICA modes are indeed spatially localised, and the second-order moments and the wall-normal correlation of some modes are localised near the wall and tend toward zero at the centre of the channel. In addition, the sizes of the ICA modes exhibit a multiscale nature and are approximately proportional to the heights. The size and height are well-defined length scales in ICA modes that neither extend to the entire region nor shrink to a point. Thus, ICA can be used as a data-driven method for localised mode decomposition. ICA modes can also reconstruct the third-order moment of the velocity fluctuations well. The sum of the third-order moments of all ICA modes is positive in the near-wall region and negative in the other region, which agrees with the DNS result and the mechanism of the most violent Reynolds shear-stress-producing events. As a comparison, the sum of the third-

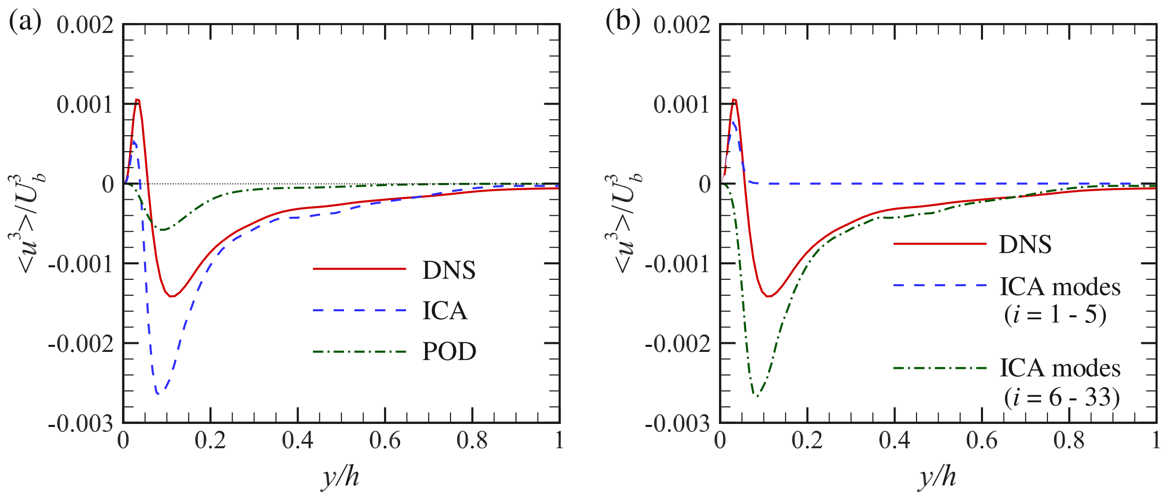

Fig. 10. (**a**) Sum of the third-order moments of all ICA modes and that of all POD modes compared with the DNS result. (**b**) Sum of the third-order moments of ICA modes with $i = 1, 2, \cdots, 5$ and with other ICA modes.

order moments of all POD modes is always negative throughout the region.

As an application of the ICA method in turbulence, this study shows that the ICA may be able to connect statistical descriptions and structural descriptions of turbulence. Future work should analyse the exact relationship between ICA modes and the attached eddy model of wall turbulence in detail.

Declaration of Competing Interest

The authors declare that they have no known competing financial interests or personal relationships that could have appeared to influence the work reported in this paper.

Acknowledgments

This work is supported by NSFC Basic Science Center Program for “Multiscale Problems in Nonlinear Mechanics” (No. 11988102) and National Natural Science Foundation of China (Nos. 12002344, 11232011 and 11572331). The authors would like to acknowledge the support from China Postdoctoral Science Foundation (No. 2020M670478), the Strategic Priority Research Program (No. XDB22040104) and the Key Research Program of Frontier Sciences of the Chinese Academy of Sciences (No. QYZDJ-SSW-SYS002).

References

[1] J.I. Cardesa, A. Velamartin, J. Jiménez, The turbulent cascade in five dimensions, Science 357 (2017) 782–784.
[2] R. Adrian, C.D. Meinhart, C. Tomkins, Vortex organization in the outer region of the turbulent boundary layer, J. Fluid Mech. 422 (2000) 1–54.
[3] X.J. Zheng, G.H. Wang, Progresses and challenges of high Reynolds number wall-bounded turbulence, Adv. Mech. 50 (2020) 202001.
[4] F. Hussain, Coherent structures and turbulence, J. Fluid Mech. 173 (1986) 303–356.
[5] J. Jiménez, Coherent structures in wall-bounded turbulence, J. Fluid Mech. 842 (2018) P1.
[6] J.C.R. Hunt, A.A. Wray, P. Moin, Eddies, streams, and convergence zones in turbulent flows, Cent. Turbul. Res. Rep., CTR-S88 (1988).
[7] M.S. Chong, A.E. Perry, B.J. Cantwell, A general classification of three-dimensional flow fields, Phys. Fluids 2 (1990) 765–777.
[8] J. Jeong, F. Hussain, On the identification of a vortex, J. Fluid Mech. 285 (1995) 69–94.
[9] P. Chakraborty, S. Balachandar, R. Adrian, On the relationships between local vortex identification schemes, J. Fluid Mech. 535 (2005) 189–214.
[10] X.H. Wu, P. Moin, Direct numerical simulation of turbulence in a nominally zero-pressure-gradient flat-plate boundary layer, J. Fluid Mech. 630 (2009) 5–41.
[11] G. Berkooz, P. Holmes, J.L. Lumley, The proper orthogonal decomposition in the analysis of turbulent flows, Annu. Rev. Fluid Mech. 25 (1993) 539–575.
[12] M. Farge, Wavelet transforms and their applications to turbulence, Annu. Rev. Fluid Mech. 24 (1992) 395–457.
[13] B. Podvin, A proper-orthogonal-decomposition-based model for the wall layer of a turbulent channel flow, Phys. Fluids 21 (2009) 015111.
[14] H. Mouri, M. Takaoka, Wavelet analysis of vortex tubes in experimental turbulence, Phys. Rev. E 65 (2002) 027302.
[15] P.J. Schmid, Dynamic mode decomposition of numerical and experimental data, J. Fluid Mech. 656 (2010) 5–28.
[16] N.E. Huang, Z. Shen, S.R. Long, et al., The empirical mode decomposition and the hilbert spectrum for nonlinear and non-stationary time series analysis, Proc. R. Soc. A 454 (1998) 903–995.
[17] L. Agostini, M.A. Leschziner, On the influence of outer large-scale structures on near-wall turbulence in channel flow, Phys. Fluids 26 (2014) 075107.
[18] L. Agostini, M.A. Leschziner, Predicting the response of small-scale near-wall turbulence to large-scale outer motions, Phys. Fluids 28 (2016) 015107.
[19] A.D. Back, A.S. Weigend, A first application of independent component analysis to extracting structure from stock returns, Int. J. Neural Syst. 8 (1997) 473–484.
[20] C. Trapnell, D. Cacchiarelli, J. Grimsby, et al., The dynamics and regulators of cell fate decisions are revealed by pseudotemporal ordering of single cells, Nat. Biotechnol. 32 (2014) 381–386.
[21] L. Carassale, Analysis of aerodynamic pressure measurements by dynamic coherent structures, Probabilist. Eng. Mech. 28 (2012) 66–74.
[22] H. Mouri, Two-point correlation in wall turbulence according to the attached-eddy hypothesis, J. Fluid Mech. 821 (2017) 343–357.
[23] P. Comon, Independent component analysis, a new concept? Signal Proc. 36 (1994) 287–314.
[24] A. Hyvärinen, E. Oja, Independent component analysis: algorithms and applications, Neural Netw. 13 (2000) 411–430.
[25] A.J. Bell, T.J. Sejnowski, An information-maximization approach to blind separation and blind deconvolution, Neural Comput. 7 (1995) 1129–1159.
[26] A. Hyvärinen, E. Oja, A fast fixed-point algorithm for independent component analysis, Neural Comput. 9 (1997) 1483–1492.
[27] L.B. Almeida, Misep - linear and nonlinear ICA based on mutual information, J. Mach. Learn. Res. 4 (2003) 1297–1318.
[28] F. Pedregosa, G. Varoquaux, A. Gramfort, et al., Scikit-learn: machine learning in python, J. Mach. Learn. Res. 12 (2011) 2825–2830.
[29] R. Penrose, On best approximate solutions of linear matrix equations, Math. Proc. Camb. 52 (1956) 17–19.
[30] T. Wu, G.W. He, Local modulated wave model for the reconstruction of space–time energy spectra in turbulent flows, J. Fluid Mech. 886 (2020) A11.
[31] J. Kim, P. Moin, R.D. Moser, Turbulence statistics in fully developed channel flow at low Reynolds number, J. Fluid Mech. 177 (1987) 133–166.
[32] A.J. Smits, B.J. Mckeon, I. Marusic, High-Reynolds number wall turbulence, Annu. Rev. Fluid Mech. 43 (2011) 353–375.